JSST
Journal of Space Science and Technology

P-ISSN: 2008-4560
E-ISSN: 2423-4516

Journal of Space Science and Technology

Vol. 18, No. 4, pp. 1-11, 2025
https://doi.org/10.22034/jsst.2025.1516
Journal Homepage: https://www.jsstpub.com

Original Research Paper

Detailed Algorithm for Implementing Robust Performance Conditions in the Presence of Saturation Nonlinearity in the QFT Framework

Hamed Kashani

Aerospace Research Institute, Ministry of Science, Research and Technology, Tehran, Iran

ARTICLE INFO

Article History:

Received 29 December 2024
Revised 09 April 2025
Accepted 30 April 2025
Available Online 11 May 2025

Keywords:

Robust control
Quantitative feedback theory
Saturation
Non-interfering architecture
Non-overshoot response

ABSTRACT

Controlling a spacecraft's orbit and attitude is one of the most complicated problems in control engineering due to uncertainties and nonlinearities. Control design methods for dealing with such issues may involve many calculations. MATLAB software automates many design methods in its control system toolbox. Many other advanced design methods must also be automated to achieve fast and accurate controller design for more complex control systems. Quantitative feedback theory (QFT), as a powerful method for addressing complex issues, requires plenty of calculations that make it necessary for the method to be automated. A QFT design toolbox is developed by the Tersoft company. However, this toolbox cannot treat some practical issues, such as actuator saturation, in its design process. In the QFT framework, saturation can be dealt with by the Horowitz architecture or non-interfering loop architecture, containing an inner loop around the saturation element in the control loop. Error overshoot is a common problem with the saturation in control loops. Non-overshoot plant input, non-overshoot plant output, and fast-vanishing plant input error are three constraints assumed in the literature to avoid this problem. These constraints can be translated to the constraints on the inner loop compensator. This paper presents a comprehensive algorithm for automating the process of obtaining the above-mentioned constraints, with detailed flowcharts to facilitate software development. To verify the proposed algorithm, the boundary on the saturation loop compensator for a hydraulic actuator is determined using computer codes implemented in the MATLAB environment. Intermediate and final results are presented to follow the calculations step by step. Finally, the validity of this boundary is checked by placing its points into the constraints mathematical expression and observing if the resultant points satisfy the constraints.

* Corresponding Author's E-mail: kashani@ari.ac.ir

How to Cite this Article:
H. Kashani, "Detailed algorithm for implementing robust performance conditions in presence of saturation nonlinearity in QFT framework," *Journal of Space Science and Technology*, Vol. 18, No. 4, pp. 1-11, 2025, https://doi.org/10.22034/jsst.2025.1516.

1. INTRODUCTION

Aerospace systems are the most complex, with various plant and environmental nonlinearity and uncertainty complexities. Attitude and orbit control systems for uncertain plants, such as space systems with large flexible structures or their components, such as nonlinear actuators, pose a quite challenging design problem in the presence of nonlinearities like actuator saturation [1-5].

One of the most powerful robust control design methods in the presence of plant uncertainty or nonlinearity is Quantitative Feedback Theory (QFT). At each frequency of interest, QFT imposes a boundary on the transfer function of the loop shaper, $G(s)$ [6]. However, in most practical problems, designing the transfer function $G(s)$ to shape the loop and determining the prefilter $F(s)$ to limit the system's frequency response within a desired boundary are not the final stages of the design process. Various practical issues, such as plant input saturation, can lead to instability and performance degradation. To address the absolute robust stability problem arising from saturation, the non-interfering architecture proposed in [7] can be employed as done in [8]. As the stability and performance requirements impose boundaries on $G(s)$ in the first stage of design, reference [7] also proposes a method to ensure the robust performance, through determining some boundaries for the inner loop compensator, $H(s)$, in the second stage of the design. In continuation of the previous work, [8], this article addresses the detailed algorithms for determining the above boundaries computationally. The algorithms facilitate the design process that involves a significant amount of calculations. Once the boundaries are determined, designing compensators that satisfy these boundaries also requires substantial effort.

The MATLAB software automates many classical control design methods [9]. Terasoft company has developed a QFT toolbox that automates the boundary calculation in the first design step [10]. Furthermore, [11] proposes a method to automate compensator synthesis in the first design stage. This paper contributes to developing an algorithm for automating the calculation of robust performance boundaries in the second design stage for saturating plant input.

In the next section, we briefly describe the suitable architecture within the QFT framework for addressing saturation in the loop. Ensuring robust performance under saturation is introduced in Section 3. The main contribution of this article is presented in section 4, which describes a detailed algorithm for implementing robust performance constraints within the QFT framework — an aspect not previously addressed in any literature. The implementation of the constraints proposed in [7], in practice, involves certain intricacies that are not mentioned in this reference or any other literature. In section 5, an illustrative example is used to examine the validity of the proposed algorithm. Finally, concluding remarks are presented in the last section of the paper.

2. Loop Architecture for Treating Saturation

The QFT framework has two main architectures for treating saturation to achieve the desired stability and performance. The first is based on Horowitz's opinion, which affects the design of $G(s)$ [12]. Another approach can be used to simplify the design process, consisting of two steps. In the first step, two controllers, $G(s)$ and $F(s)$, are designed using a common QFT design procedure, ignoring the saturation. In the second step, controller $H(s)$ is designed to reduce the undesired effects of plant input saturation. Fig. 1 shows this non-interfering architecture for addressing saturation in the plant input [13]. The term "non-interfering" is used because the compensator $H(s)$ is not active until the plant input saturates. According to this architecture, the loop transmission around the saturation element, L_n, can be written as follows.

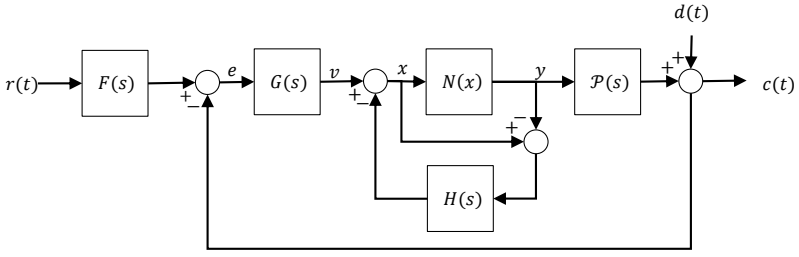

Fig. 1. Non-interfering control architecture [5].

$$L_n = -\frac{X}{Y} = \frac{L-H}{1+H} \quad (1)$$

therefore,

$$H = \frac{L-L_n}{1+L_n} \quad (2)$$

where, $L = GP$.

To ensure robust performance, H(s) must satisfy constraints of fast-vanishing plant input error (FVIE), non-overshoot plant input error (NOIE), and non-overshoot plant output error (NOOE) [5].

3. Conditions for Robust Performance

As expressed in [7], the following three conditions determine the closeness of the saturated system response to the unsaturated one: FVIE, $e_y = y^i - y_l^i$, NOIE, and NOOE $e_c = c^i - c_l^i$. In the presence of uncertainty, this closeness is referred to as robust performance.

3.1 Fast-vanishing plant input error

The plant input error, e_y, represents the difference between the plant input in a non-saturating ideal loop and that in a loop that contains saturation, as defined in the Horowitz methodology [12]. This error approaches zero through the dynamics of $1/(1+L_n)$ in response to excitation $\left[l_n * \left(y_{l_i} - y_i\right)\right]^i$. The vanishing rate of e_y is assessed with the rate of change of y_l that arises from the dynamics of $L(j\omega)$. Therefore, a FVIE condition requires that $\omega_{c_{L_n}} > \omega_{c_L}$, where $\omega_{c_{L_n}}$ and ω_{c_L} represent the crossover frequencies of L_n and L, respectively. This requirement implies that $|L_n(j\omega)| > 1$ for $0 < \omega < \beta\omega_{c_L}$ where $\beta > 1$. By utilizing Eq. (2) to translate the constraint $|L_n(j\omega)| > 1$ into a constraint on $H(j\omega) = \mathcal{R}_H(\omega) + j\mathcal{I}_H(\omega)$, when $L(j\omega) = \mathcal{R}_L(\omega) + j\mathcal{I}_L(\omega)$, the following inequalities can be derived.

$$\begin{cases} \mathcal{I}_H < -\dfrac{1+\mathcal{R}_L}{\mathcal{I}_L}\mathcal{R}_H - \dfrac{1-\mathcal{R}_L^2-\mathcal{I}_L^2}{2\mathcal{I}_L} & \mathcal{I}_L > 0 \\ \mathcal{I}_H > -\dfrac{1+\mathcal{R}_L}{\mathcal{I}_L}\mathcal{R}_H - \dfrac{1-\mathcal{R}_L^2-\mathcal{I}_L^2}{2\mathcal{I}_L} & \mathcal{I}_L < 0 \end{cases} ; \quad 0 < \omega < \beta\omega_{c_L} \text{where } \beta > 1 \quad (3)$$

At each frequency, these linear inequalities define a region in the Nyquist plane that is bounded by a set of intersecting lines associated with the variations in the plant. This region can be transformed into the Nichols plane to facilitate the design of $H(j\omega)$ while ensuring a FVIE, using the method described in [8].

3.2 Non-overshoot plant input error

Equation (4) expresses the NOIE condition for the loop shown in Fig. 1 as follows [7].

$$\left|\frac{L_n(j\omega)}{1+L_n(j\omega)}\right| < \gamma_i(\omega) \quad (4)$$

The plant input error does not overshoot if $\gamma_i(\omega) \leq 1$. Using Eq. (1) in Eq. (4) converts the condition on L_n to the condition (5) on H.

$$\left|\frac{L-H}{1+L}\right| = \left|\frac{(\mathcal{R}_L-\mathcal{R}_H)+\mathbb{i}(\mathcal{I}_L-\mathcal{I}_H)}{(1+\mathcal{R}_L)+\mathbb{i}\mathcal{I}_L}\right| < \gamma_i(\omega) \quad (5)$$

Therefore,

$$\frac{(\mathcal{R}_L-\mathcal{R}_H)^2+(\mathcal{I}_L-\mathcal{I}_H)^2}{(1+\mathcal{R}_L)^2+\mathcal{I}_L^2} < \gamma_i^2(\omega) \quad (6)$$

finally,

$$(\mathcal{R}_H-\mathcal{R}_L)^2+(\mathcal{I}_H-\mathcal{I}_L)^2 < \gamma_i^2((1+\mathcal{R}_L)^2+\mathcal{I}_L^2) = \Gamma_i^2 \quad (7)$$

For specified plant parameters, the above constraint forms a circle with radius $\Gamma_i = \gamma_i\sqrt{((1+\mathcal{R}_L)^2+\mathcal{I}_L^2)}$ and center $[\mathcal{R}_L, \mathcal{I}_L]$. As shown in Fig. 2, there are two cases depending on whether this circle contains the origin of the Nyquist plane. In the first case, the projection of the constraint onto the Nichols plane is an open boundary that spans from $-360°$ to $0°$. In the second case, the projection is a closed boundary

within a specified range of the phase axis of the Nichols plane, $\phi_1 \le \phi \le \phi_2$.

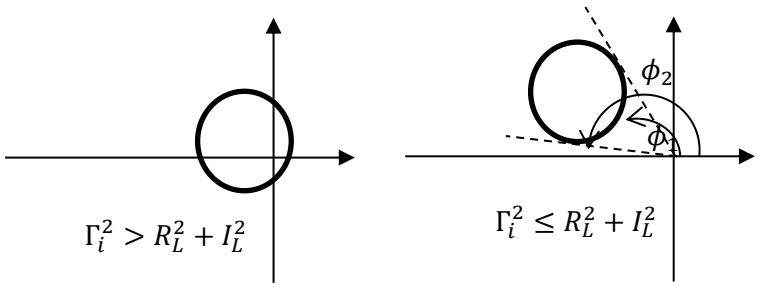

Fig. 2. Nyquist schematic plot of the constraint on H to have NOIE.

In the presence of uncertainty, at a specified frequency, each plant variant imposes a constraint on H as described above. Therefore, the admissible region in the Nyquist plan will be the area bounded by the intersection of all these individual regions.

3.3 Non-overshoot plant output error

The following inequality mathematically expresses the condition for a NOOE [7].

$$\left|\frac{P}{1+L_n}\right| = \left|\frac{P(1+H)}{1+L}\right| < \gamma_o(\omega) \qquad (8)$$

Using the real and imaginary parts of each transfer function leads to the following expression.

$$\frac{(\mathcal{R}_P^2 + \mathcal{I}_P^2)((1+\mathcal{R}_H)^2 + \mathcal{I}_H^2)}{(1+\mathcal{R}_L)^2 + \mathcal{I}_L^2} < \gamma_o^2 \qquad (9)$$

finally,

$$(\mathcal{R}_H + 1)^2 + \mathcal{I}_H^2 < \gamma_o^2 \frac{(1+\mathcal{R}_L)^2 + \mathcal{I}_L^2}{\mathcal{R}_P^2 + \mathcal{I}_P^2} = \Gamma_o^2 \qquad (10)$$

At each frequency, the constraint (10) represents a region enclosed by a circle of radius $\Gamma_i = \gamma_o^2\,((1+\mathcal{R}_L)^2 + \mathcal{I}_L^2)/(\mathcal{R}_P^2 + \mathcal{I}_P^2)$ and centered at $[-1,0]$ in the Nyquist plan. As shown in Fig. 3, there are two cases, whether this circle contains the origin of the Nyquist plan or not. In the first case, the projection of the constraint on the Nichols plan is the region below an open boundary extending from $-360°$ to $0°$, while in the second case, the projection is the region enclosed by a closed boundary within a specified range of phase axis of the Nichols plan, $\phi_1 \le \phi \le \phi_2$.

In the presence of uncertainty, at a specified frequency, since all circles of constraints are concentric, the admissible region is that enclosed by the smallest circle. The projection of this region onto the Nichols plan will be the area below a boundary extending from $-360°$ to $0°$ if the origin in the Nyquist plan lies within the admissible area. Otherwise, it will be the interior of a closed region within a specified range of the phase axis, $\phi_1 \le \phi \le \phi_2$.

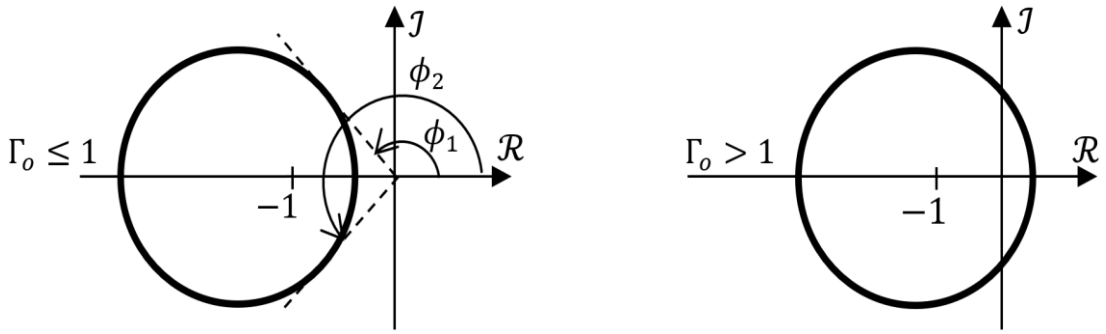

Fig. 3. Nyquist schematic plot of constraint on H to have NOOE.

4. Algorithm Development

Imposing the above-mentioned constraint on the inner loop compensator, even for simple systems with limited dimensions, requires an extensive numerical computation cost. The following section provides the algorithms to develop the computer codes for automating the process of design boundary generation.

4.1 Fast-vanishing plant input error

The constraint (3) for FVIE is similar to the constraint of the circle criterion for absolute robust stability, discussed in reference [8]. Therefore, the reader can refer to this paper for details.

4.2 Non-overshoot plant input error

At a specified frequency, in the presence of uncertainty, the NOIE condition (7) is satisfied within the region of intersection of all circles related to plant variants, in the Nyquist plan. Here, at first, the boundary of the admissible region is calculated, and then this boundary will be transformed into the Nichols plan.

Fig. 4 shows the calculation process flowchart of the boundary of the intersection of all circles associated with the plant variants at a specified frequency. The overall logic of this flowchart is to select a circle and, with a desired resolution, check whether its peripheral points lie within all other circles. The points that satisfy this condition are stored in an array. The process is repeated for the other circles. By doing the same for the last circle, the boundary points of the admissible region are gathered in an array.

In the next step, the boundary calculated above should be transformed to the Nichols plan. As previously expressed, if the origin of the Nyquist plan lies within the admissible region, then its projection onto the Nichols plan will be part of the Nichols plan under the open boundary, extended along all of phase axes. The projection of the admissible region onto the Nichols plan will form a closed area limited to the phase strip of $\phi_1 \leq \phi \leq \phi_2$ as schematically shown in the right-hand plot of Fig. 2. It is important to note that this plot is drawn for one of the circle constraints, but here, we are considering the boundary of the area of circles intersection.

The projection of the admissible area from the Nyquist plan to the Nichols plan requires that the array containing the points of the final boundary on the Nyquist plan be expressed in phase-modulus representation. The expressing can become complicated if the admissible region has concave shape, as shown in Fig. 5. Concavity imposes many considerations that must be taken into account when finding the intersection points and determining the admissible sections indicated by the solid line segments in Fig. 5. Fortunately, it can be demonstrated that the intersection of a number of circles will not have a concave form.

Lemma: The intersection of multiple circles always forms a convex shape.

Proof: The intersection of multiple circles always forms a convex shape. This is because the concavity of the intersection can only occur at the edge or corner of the intersecting area. For edge concavity, as shown in Fig. 6a, the outer area of the circle, “A”, that contributes to the concave edge should be part of the admissible region, which is a contradiction. Similarly, for the corner concavity as shown in Fig. 6 b, two uncommon parts of two circles “A” and “B” would contribute to the intersection, which is impossible.

Mapping the boundary of the admissible region from the Nyquist plan to the Nichols plan in the case where the origin does not lie within the admissible region requires, initially, a transformation in the Nyquist plan to include the origin within the admissible region. This transformation helps produce a sorted array of boundary points for plotting the admissible region on the Nichols plan. To this end, the origin is transformed to a point within the admissible region, with its coordinates obtained by taking the simple average of the abscissa and ordinate of the boundary points. The convexity of the admissible region guarantees that this point will not lie outside the region.

The next step involves converting the coordinates of the boundary points from Cartesian to polar, followed by sorting them according to their phase angles. The sorted points are then converted back to Cartesian coordinates with respect to the original origin. Finally, the resultant boundary points' coordinates are transformed into phase-modulus information to represent the boundary on the Nichols plan. A detailed algorithm for code generation is presented in Fig. 7.

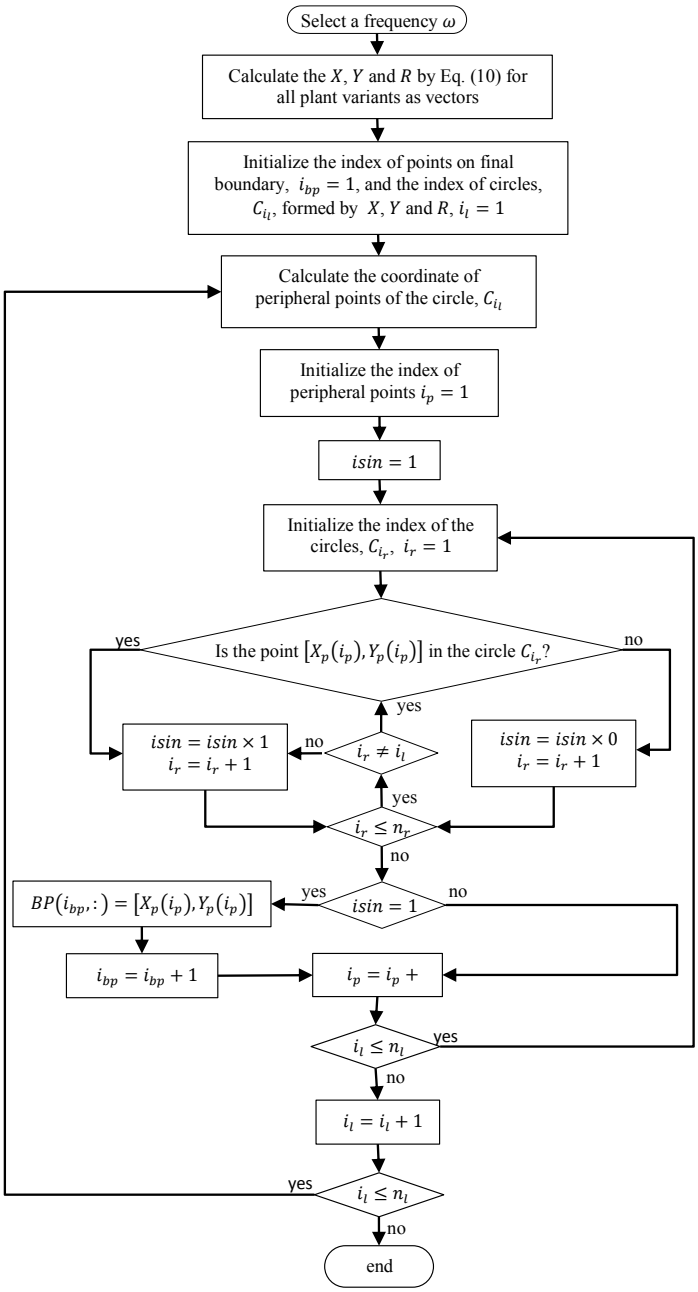

Fig. 4. Flowchart for calculating the boundary of the NOIE constraint.

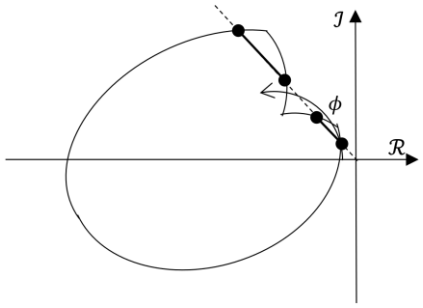

Fig. 5. The concave admissible region and the resulting complexity of mapping from the Nyquist plan to the Nichols plan.

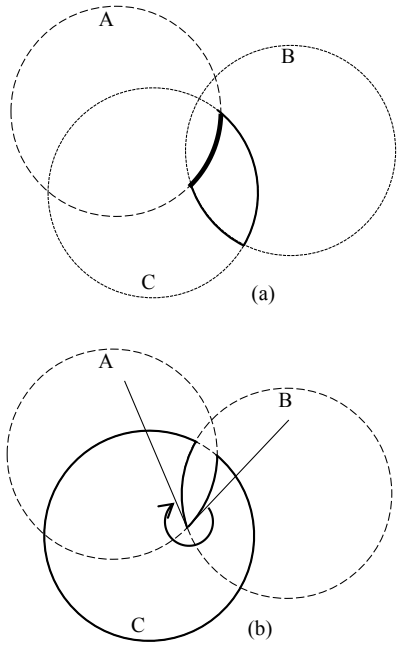

Fig. 6. Impossibility of a concave multiple circle edge and corner concavity.

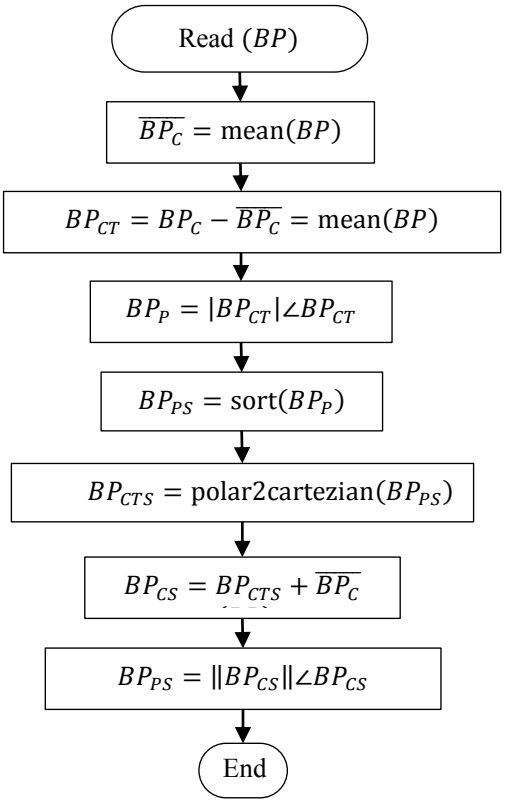

Fig. 7. Flowchart for mapping the admissible region from the Nyquist plan to the Nichols plan.

4.3 Non-overshoot plant output error

The last robust performance criterion implies the non-overshoot condition on the plant output error. It can be translated into the constraint on the controller $H(s)$, as expressed by Eq. (10). As shown in Fig. 3 for all plant variants, all circles representing the constraints are concentric. Therefore, the smallest circle will be the final boundary in the Nyquist plan. The geometry of this case is a special form of the previous case, and the algorithm presented in Fig. 7 may be utilized to map the admissible region–that is, the area encircled by the smallest circle–from the Nyquist plan to the Nichols plan.

5. Example and Algorithms Verification

A wide variety of actuators, including electromechanical, electromagnetic, and electrohydraulic types, are used in space applications. To examine the validity of the proposed algorithm, an electrohydraulic actuator is considered here. The transfer function of the hydraulic actuator, given by Eq. (11), is a customized form employed in [14], with inertial terms ignored and some differences in the numerical values of parameters. This transfer function, with actuator force as the output and excitation voltage as the input, is used for the algorithm verification process. Saturation manifests in this plant as a limitation of the excitation voltage to 24 v.

$$P = \frac{K_s(A_i + A_o)}{R} \frac{(d + d_e)s + k_e}{D_3 s^3 + D_2 s^2 + D_1 s + D_0} \tag{11}$$

where,

$$\begin{aligned} D_0 &= K_p k_e \\ D_1 &= A_i^2 + A_o^2 + K_p(d + d_e) + Ck_e + k_e K_p \tau \\ D_2 &= (A_i^2 + A_o^2)\tau + (C + K_p \tau)(d + d_e) + Ck_e \tau \\ D_3 &= C(d + d_e)\tau \end{aligned} \tag{12}$$

Additionally, $A_i = 855\ mm^2$, $A_o = 428\ mm^2$, $d = 200\ \ Ns/m^2$, $d_e = 100\ \ Ns/m^2$ and R=28 Ω represent the piston's extending side area, piston's retracting side area, damping coefficient of the cylinder-piston contact region, damping coefficient of the load, and electrical resistance of the proportional valve solenoid, respectively. The other parameters vary within the ranges listed in Table 1.

As the first stage of the design process, the nominal values listed in this table are used to shape the loop using the QFT method, resulting in the following transfer function for the loop transmission $L_0 = GP_0$. Details of this design stage

are not presented for brevity, and readers can refer to [14] for more information.

$$L_0 = 10^7 \frac{7.2s^3+6.7\times10^2s^2+1.7\times10^4s+4.4\times10^4}{s^5+4\times10^4s^4+10^6s^3+2.6\times10^7s^2+1.3\times10^7s} \quad (13)$$

The degrees of the numerator and denominator of L are the same as those of L_0, but their coefficients vary depending on changes in the plant parameters. Assuming only the lower and upper limits of parameter variations listed in Table 1, there are 32 possible plant variants. $H(s)$ must be designed to satisfy the conditions of robust performance.

By implementing the flowcharts developed here and in [8] for frequencies $\omega = 0.1\ rad/s$, $\omega = 50\ rad/s$ and $\omega = 600\ rad/s$, boundaries related to each of the robust performance conditions are obtained. At first, the condition of the FVIE is examined.

5.1 Fast vanishing plant input error

As mentioned previously, the condition of FVIE is similar to the condition of the circle criterion for robust absolute stability. Therefore, employing the algorithm developed in [8] leads to the boundaries in the Nyquist and Nichols plans, as shown in the first and second rows of Fig. 8, respectively. In the Nyquist plan, as indicated by the files' black triangle markers, the region above the solid broken line is the admissible region. In the Nichols plan, black and gray curves indicate the upper and lower boundaries, respectively. As seen in the Nichols plots, the compensator $H(s)$ has not been subjected to any lower limitations at frequencies of $\omega = 0.1\ rad/s$ and $\omega = 50\ rad/s$.

For validation, breaking points of the overall boundary in the Nyquist plan are selected as testing points and used to generate associated points on $L_n(j\omega)$ according to Eq. (1). For all variants of the plant at 16 frequencies in the range $0.1 \le \omega \le 600\ rad/s$, $L_n(j\omega)$ scatters in the Nyquist plan, as shown in Fig. 9. In part (a) of this figure, all points associated with all plant variants at 16 frequencies are presented. However, due to scale inconsistency, the circle of unit radius is not visible in this part of the figure. Part (b) of this figure presents a magnified view of part (a) in the vicinity of the origin of the Nyquist plane. As seen, there is no scattering of points in the region within the circle of unit radius. The absence of scattering points in the circle of unit radius indicates that the algorithm correctly calculates the boundaries of the FVIE condition.

Table 1. Nominal value and variation range of the plant parameters.

Parameter	Description	Nominal value	Range
k_e	Load stiffness	$5\times10^5[N/m]$	[267,985000]
K_i	Flow rate sensitivity to excitation current	$1.5\times10^{-3}[m^3/As]$	$[1,2]\ \times10^{-3}$
K_p	Flow rate sensitivity to pressure difference	$-65\times10^{-12}\ [m^2/sPa]$	$[-65,2650]\times10^{-12}$
C	Flow rate sensitivity to pressure rate	10.7×10^{-15}	$[8.56,12.83]\times10^{-15}$
τ	Solenoid time constant	$22.5\ ms$	[20,25]

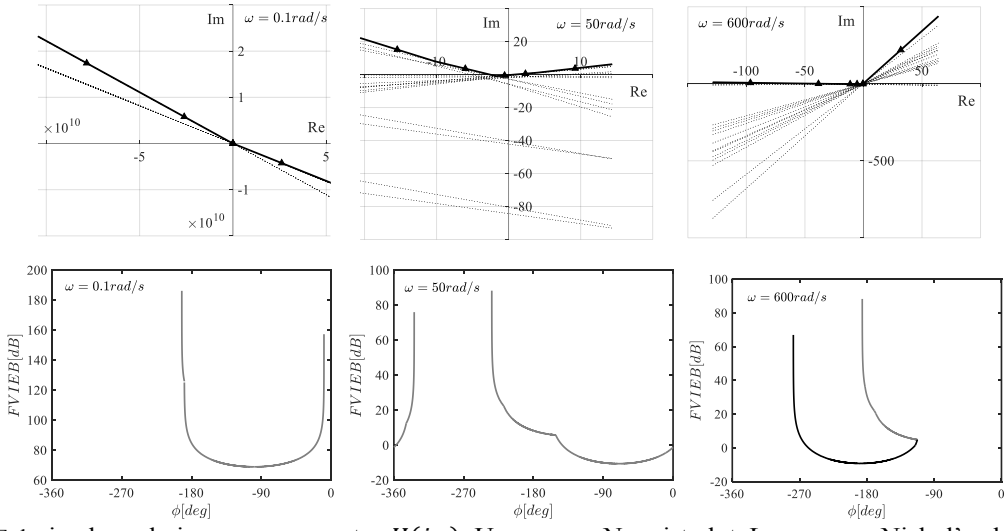

Fig. 8. FVIE design boundaries on compensator $H(j\omega)$, Upper row: Nyquist plot, Lower row: Nichol's plot; Black and gray curves represent the lower and upper boundaries, respectively.

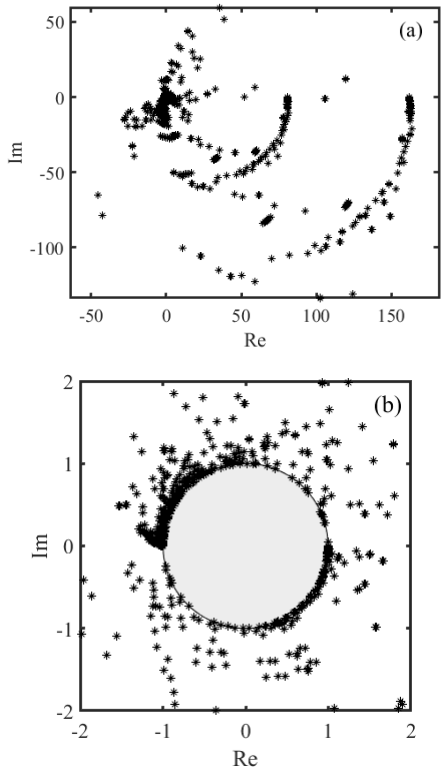

Fig. 9. Examining the algorithm of FVIE by direct check of the $L_n(\omega)$ in the Nyquist plan.

5.2 Non-overshoot plant input error

Employing the algorithm developed to determine the boundaries imposed by the NOIE condition on the compensator $H(s)$ for the examining example with $\gamma_i = 1$, leads to boundaries in the Nyquist and Nichols plans, shown in the first and second rows of Fig. 10, respectively.

To check if these obtained boundaries result in $|L_n/(1+L_n)| < \gamma_i$, some boundary points are selected and substituted into Eq. (1) for all plant variants to calculate L_n and then $L_n/(1+L_n)$. Figure 11 presents the scatter pattern of $L_n/(1+L_n)$. It can be seen that all points lie within a circle of radius $\gamma_i = 1$ centered at the origin of the Nyquist plan. Therefore, the calculated boundaries in Fig. 10 satisfy the condition of NOIE.

5.3 Non-overshoot plant output error

Finally, the algorithm developed to implement the condition of NOOE is evaluated by utilizing it for the examining example. Figure 12 presents two rows of plots. These rows represent the calculated design boundaries of the compensator $H(s)$ for selected frequencies in the Nyquist and Nichols planes, respectively. Boundaries associated with each plant variant and the resultant one are shown together in the case of the Nyquist boundary representation. The Nichols plan boundary for the frequency of $\omega = 0.1\ rad/s$ is an open upper boundary, while for the other two frequencies, the boundaries are closed.

To ensure that the calculated boundaries are correct, selected points are substituted into Eq. (8) for $\gamma_o = 1$. As seen in Fig. 11, the condition of NOOE is satisfied for all plant variants over the desired frequency range.

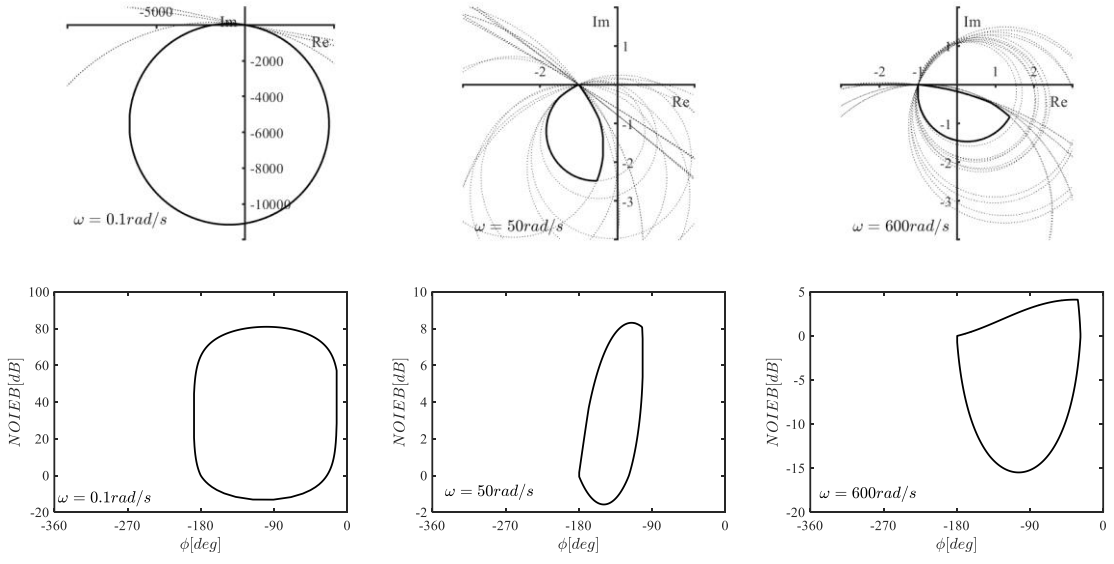

Fig. 10. NOIE design boundaries on compensator $H(j\omega)$, Upper row: Nyquist plot, Lower row: Nichol's plot.

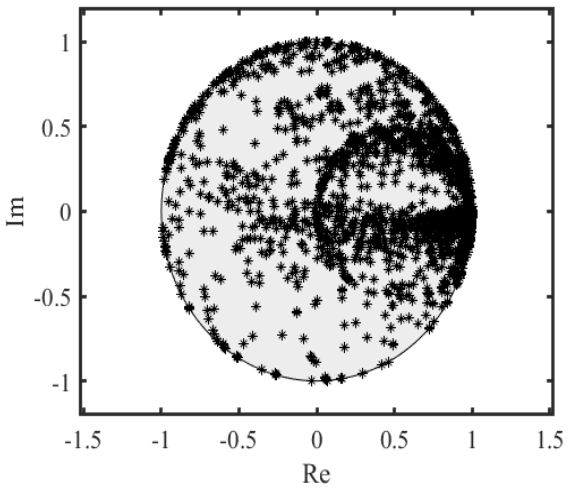

Fig. 11. Examining the algorithm of NOIE by direct check of the $L_n/(1+L_n)$ in the Nyquist plan.

6. Conclusion

QFT is a powerful and robust tool for designing controllers in the presence of plant uncertainty and input saturation, which are prevalent in space systems and components. One approach to address this involves a non-interfering control loop architecture.

First, a robust linear controller is designed through loop shaping and prefiltering, initially disregarding saturation. Subsequently, a loop is constructed around the saturation element to mitigate its undesired effects. Robust stability in this architecture relies on satisfying the circle criterion, as investigated by [8]. However, robust stability alone is insufficient. This article considers the numerical implementation of three additional conditions to ensure robust performance: FVIE, NOIE, and NOOE.

To automate the implementation of these robust performance conditions, this paper presents detailed algorithms. Flowcharts are provided to facilitate the generation of computer code for these algorithms.

An example demonstrates the application of these algorithms, presenting intermediate and final results to track the process. Finally, direct validation confirms that the calculated overall boundaries satisfy the robust performance conditions.

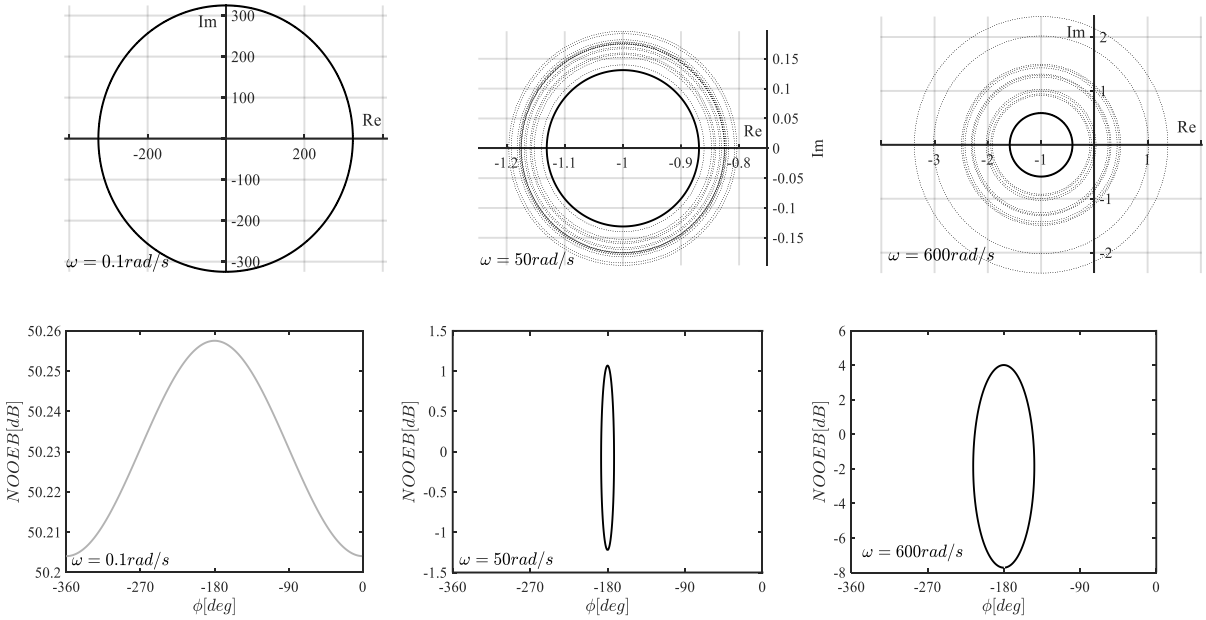

Fig. 12. NOOE design boundaries on compensator $H(j\omega)$, Upper row: Nyquist plot, Lower row: Nichol's plot.

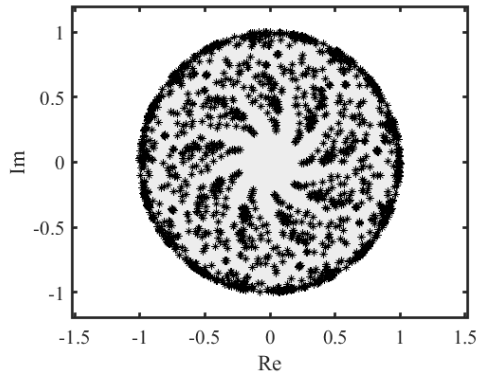

Fig. 13. Examining the algorithm of NOOE by direct check of the $P/(1+L_n)$ in the Nyquist plan.

CONFLICTS OF INTEREST

The authors declare that they have no conflict of interest.

REFERENCES

[1]W. H. Chen, "QFT design for spacecraft with uncertain flexible structures," in *6th World Congress on Intelligent Control and Automation*, Dalian, China, 2006, pp. 8191-8195, https://doi.org/10.1109/WCICA.2006.1713571.

[2]M. V. Chitra, K. K. Sharma, and A. A. Kumar, "Quantitative feedback theory-based robust control design for a flexible launch vehicle," in *International Conference on Control Communication & Computing India (ICCC)*, Trivandrum, India, 2015, pp. 72-77, https://doi.org/10.1109/ICCC.2015.7432872.

[3]M. Garcia Sanz, I. Eguinoa, M. Barreras, and S. Bennani, "Nondiagonal MIMO QFT controller design for Darwin-type spacecraft with large flimsy appendages," *Journal of Dynamic Systems, Measurement and Control,* vol. 130, no. 1, 2008, Art. no. 011006, https://doi.org/10.1115/1.2807067.

[4]A. Sinha, S. P. Chakravarty, P. Dutta, and P. Roy, "Attitude and vibration control of a solar paneled satellite using quantitative feedback theory-based robust controller," in *Control and Measurement Applications for Smart Grid*, *Select Proceedings of SGESC 2021*, S. Suhag, C. Mahanta, and S. Mishra, Eds. Singapore: Springer, 2022, pp. 155-165, https://doi.org/10.1007/978-981-16-7664-2_13.

[5]Z. Li, W. Zhou, and H. Liu, "Robust controller design of non-minimum phase hypersonic aircraft model based on quantitative feedback theory," *Journal of the Astronautical Sciences,* vol. 67, pp. 137-163, 2020, https://doi.org/10.1007/s40295-019-00187-y.

[6]C. H. Houpis, S. J. Rasmussen, and M. Garcia-Sanz, *Quantitative Feedback Theory, Fundamentals and Applications*, 2nd Ed. Boca Raton: CRC Press, 2005, https://doi.org/10.1201/9781315219301.

[7]W. Wu, S. Jayasuriya, and M. H. Kotzebue, "A new QFT design methodology for feedback systems under input saturation," *Journal of Dynamic Systems, Measurement and Control*, vol. 123, no. 2, pp. 225-232, 2001, https://doi.org/10.1115/1.1367337.

[8]H. Kashani, "Detailed algorithm for implementing circle criterion in QFT framework for saturation nonlinearity," *Journal of Space Science and Technology*, vol. 17, Special issue, pp. 32-44, https://doi.org/10.22034/jsst.2024.1497.

[9]"Control System Toolbox," [Online]. Available: https://www.mathworks.com/products/control.html

[10]C. Borghesani, Y. Chait, and O. Yaniv, *The QFT Frequency Domain Control Design Toolbox*, User's Guide, Terasoft, Inc., 2003.

[11]M. García Sanz and J. A. Osés, "Evolutionary algorithms for automatic tuning of QFT controllers," in *IASTED International Conference on Modelling, Identification and Control*, Switzerland, 2004.

[12]I. M. Horowitz, "A synthesis theory for a class of saturating systems," *International Journal of Control*, vol. 38, no. 1, pp. 169-187, 2007, https://doi.org/10.1080/00207178308933067.

[13]W. Wu and S. Jayasuriya, "Controller design for a nonovershooting step response with saturating nonlinearities," in *American Control Conference*, San Diego, CA, USA, 1999, pp. 3046-3050, https://doi.org/10.1109/ACC.1999.782321.

[14]N. Niksefat and N. Sepehri, "Design and experimental evaluation of a robust force controller for an electro-hydraulic actuator via quantitative feedback theory," *Control Engineering Practice*, vol. 8, no. 12, pp. 1335-1345, 2000, https://doi.org/10.1016/S0967-0661(00)00075-7.